Geophysical Research Letters

RESEARCH LETTER
10.1029/2021GL096835

Key Points:

- Non-intrusive method to map the full three-dimensional time-averaged pressure field in full-scale flume experiments
- Water surface identification from reconstructed pressure distribution from measured velocity field
- Hyporheic fluxes induced by a barely submerged single stem are stronger than those from dune-like bedforms in equilibrium with the flow

Supporting Information:

Supporting Information may be found in the online version of this article.

Correspondence to:

D. Tonina,
dtonina@uidaho.edu

Citation:

Moreto, J. R., Reeder, W. J., Budwig, R., Tonina, D., & Liu, X. (2022). Experimentally mapping water surface elevation, velocity and, pressure fields of an open channel flow around a stalk. *Geophysical Research Letters*, *49*, e2021GL096835. https://doi.org/10.1029/2021GL096835

Received 29 OCT 2021
Accepted 9 MAR 2022

Author Contributions:

Conceptualization: Daniele Tonina, Xiaofeng Liu
Data curation: William Jeff Reeder
Formal analysis: Jose Roberto Moreto, William Jeff Reeder, Xiaofeng Liu
Funding acquisition: Ralph Budwig, Daniele Tonina, Xiaofeng Liu
Investigation: Jose Roberto Moreto, William Jeff Reeder
Methodology: Jose Roberto Moreto, William Jeff Reeder, Ralph Budwig, Daniele Tonina, Xiaofeng Liu
Project Administration: Daniele Tonina
Resources: Ralph Budwig, Daniele Tonina, Xiaofeng Liu
Software: Jose Roberto Moreto, Xiaofeng Liu
Validation: Xiaofeng Liu
Visualization: Jose Roberto Moreto, Xiaofeng Liu

Experimentally Mapping Water Surface Elevation, Velocity, and Pressure Fields of an Open Channel Flow Around a Stalk

Jose Roberto Moreto[1], William Jeff Reeder[2], Ralph Budwig[2], Daniele Tonina[2], and Xiaofeng Liu[1]

[1]Department of Aerospace Engineering, San Diego State University, San Diego, CA, USA, [2]Center for Ecohydraulics Research, University of Idaho, Boise, ID, USA

Abstract Quantification of velocity and pressure fields over streambeds is important for predicting sediment mobility, benthic and hyporheic habitat qualities, and hyporheic exchange. Here, we report the first experimental investigation of reconstructed water surface elevations and three-dimensional time-averaged velocity and pressure fields quantified with non-invasive image techniques for a three-dimensional free surface flow around a barely submerged vertical cylinder over a plane bed of coarse granular sediment in a full-scale flume experiment. Stereo particle image velocimetry coupled with a refractive index-matched fluid measured velocity data at multiple closely-spaced parallel and aligned planes. The time-averaged pressure field was reconstructed using the Rotating Parallel Ray Omni-Directional integration method to integrate the pressure gradient terms obtained by the balance of all the Reynolds-Averaged Navier-Stokes equation terms, which were evaluated with stereo particle image velocimetry. The detailed pressure field allows deriving the water surface profile deformed by the cylinder and hyporheic flows induced by the cylinder.

Plain Language Summary This paper presents the first experiment that measured the pressure distribution around an object representing the stem of a plant placed over a rough surface made of irregular particles and barely covered by moving water using image analysis. Calculating the pressure distribution in moving water in a channel is challenging because the pressure caused by the weight of the water is much larger than that caused by the moving water. The presence of waves on the water surface and the irregular bed surface formed by sediment grains makes the analysis even more complex as the conditions near these locations are difficult to determine. Here, we used an object made of a transparent material that makes it invisible within water mixed with Epsom salt. This allows image analysis to measure water velocity from which we derived the pressure distributions everywhere in the water. By having the water surface within the image, we were able to reconstruct the water surface from the pressure field as pressure nears atmospheric value at that position. Knowing the near-bed pressure distribution allowed us to predict the amount of water that is driven into the voids among the grains due to the presence of the object.

1. Introduction

Surface (in-stream waters) hydraulics have important implication for both surface (Marion et al., 2015) and sub-surface (groundwater) hyporheic zone biogeochemical (Quick et al., 2016; Zarnetske et al., 2011) and ecological (Peralta-Maraver et al., 2018; Tonina & Buffington, 2009; Ziebis et al., 1996) processes, besides governing hyporheic fluxes (Boano et al., 2014). Hyporheic fluxes are surface water that is advectively pumped in and out of the streambed sediment mainly due to near-bed pressure distributions, which form the ubiquitous hyporheic exchange between surface and streambed pore water. Downwelling fluxes transfer solutes and surface water into the sediment that sustain and influence pore habitats and ecosystems (Kim et al., 1992). Biofilms attached to grain surfaces and organisms dwelling within grain interstices uptake solutes and release transformed products, which are carried away by the hyporheic flow and into the stream by upwelling hyporheic waters (Bott et al., 1984; Triska et al., 1993). These biogeochemical and transport processes cause concentration gradients that sustain a rich ecotone (Edwards, 1998; Gibert et al., 1994) and depend on water temperature, solute concentrations, subsurface flow velocity, and flow path lengths (Findlay et al., 1993; Ocampo et al., 2006). The effect of local hyporheic processes goes beyond the single reach as it impact stream surface water quality (Fischer et al., 2005) and also emissions of greenhouse gases (Marzadri et al., 2017).

Writing – original draft: Daniele Tonina
Writing – review & editing: Jose Roberto Moreto, William Jeff Reeder, Ralph Budwig, Daniele Tonina, Xiaofeng Liu

Surface water flow fields around objects in open channel flows can be directly measured with high precision invasive, for example, acoustic doppler velocimeters, and non-invasive methods, for example, image techniques such as particle image velocimetry (PIV) (Blois et al., 2014). However, pressure fields especially the near-bed pressure distribution are complex (Shen et al., 2020; Voermans et al., 2017) and difficult to measure with direct techniques such as piezometers, pressure transducers or Pitot tubes, because of small magnitude variations riding on top of a large hydrostatic pressure field (Fehlman, 1985). This is true in both field and laboratory settings. In the latter case, non-intrusive image analysis techniques like stereo PIV (SPIV) allow detailed and high-resolution measurements of the flow field at the turbulence time scale (Westerweel et al., 2013). This information has allowed development of methods to reconstruct both turbulence averaged (Gurka et al., 1999; van Oudheusden, 2013) and instantaneous pressure (Liu & Katz, 2006) fields from the fluid governing equation in case of well-defined and geometrically-simple domains (De Kat & Van Oudheusden, 2012; Liu & Katz, 2006; van Oudheusden, 2013). SPIV has the advantage of being non-intrusive and providing the instantaneous three velocity components along with accurate quantification of their uncertainties. However, being an optical method, it relies on "seeing" the flow within the entire area of interest. This is not possible in case of most solid objects immersed in the fluid, because, even if they are transparent but have different refraction index from the fluid, they cause shadows or partially/fully block the view of the flow. To avoid this problem, laboratory experiments use refractive index matching (RIM) techniques (Budwig, 1994; Weitzman et al., 2014), in which both solid and fluid exhibit similar optical properties (e.g., similar values in their indices of refraction, and their transmittance, etc.), such that they are virtually indistinguishable (Figure 1b), that is, the solid is functionally transparent, and SPIV can see through the solid and map the flow field all around it (Voermans et al., 2017). Application of this technique is typically expensive and/or hazardous (but see, Weitzman et al., 2014), because of the use of specialized and toxic liquids coupled with commonly used transparent solid materials, typically glass (Budwig, 1994). Thus, most laboratory RIM coupled SPIV applications are for small-scale experiments (e.g., Kim et al., 2020; Rousseau & Ancey, 2020).

The pressure field is then reconstructed from SPIV velocity data by first locally applying the momentum (Navier-Stokes) equations in differential form and successively integrating the pressure gradient to obtain the pressure field. This pressure reconstruction has been shown to be effective in several previous works (De Kat & Van Oudheusden, 2012; Joshi et al., 2014; Liu & Katz, 2006, 2008; 2013) studying mainly two-dimensional flows. However, those applications were performed in closed domains with geometries with smooth, well-defined, and known boundaries, for example, smooth walls and without water surface elevation, whose location changes spatially, and without large solid bodies protruding within the flow. However, such protrusions are typical in experimental studies of flows over coarse sediments with large macro-roughness elements, such as boulders, bedforms and aquatic vegetation, which depending on their submergence may cause complex water surface elevation patterns (Nepf, 2012). Here, we present the first real-scale three-dimensional open flow experimental investigation of the time-averaged pressure field around a barely submerged vertical cylinder, which mimics a single rigid stem of aquatic vegetation over a rough bed, and its implication in driving hyporheic exchange, and its influence on the corresponding surface elevation shape variation. We selected a barely submergenced condition, which is considered as emergent vegetation as the water depth is similar to the stalk height (Nepf, 2012), because it is a critical situation with important water surface deformation around the stem.

2. Method

2.1. Experimental Set Up

We ran a 10 L s^{-1} discharge in a 7 m long, 0.5 m wide and 0.7 m deep tilting and recirculating flume over a 5 cm deep porous bed made of crashed glass particles with 3 mm median size (Figure 1a and Figure S1 in Supporting Information S1). The established flow had 0.2 m s^{-1} mean velocity and depth of 0.1 m with Reynolds and Froude numbers of nearly 19,000 and 0.2, respectively. The flow passed through a diffuser and flow straightener before entering the flume and before reaching the stalk, located in the center of the middle third of the flume (~3.5 m from the upstream flume end). The stalk was 0.1 m tall with a 0.01 m diameter, D, and was made of transparent polymer (3M® THV 221-GZ) with specific gravity of nearly 2 and refractive index of 1.365 similar to that of water (1.33) (Hilliard et al., 2021). To match refractive indices, we added 15% in weight of $MgSO_4$ (Epsom salt) to the water. The resulting salt solution is non-toxic and relatively inexpensive with a density of 1,157 kg/m^3,

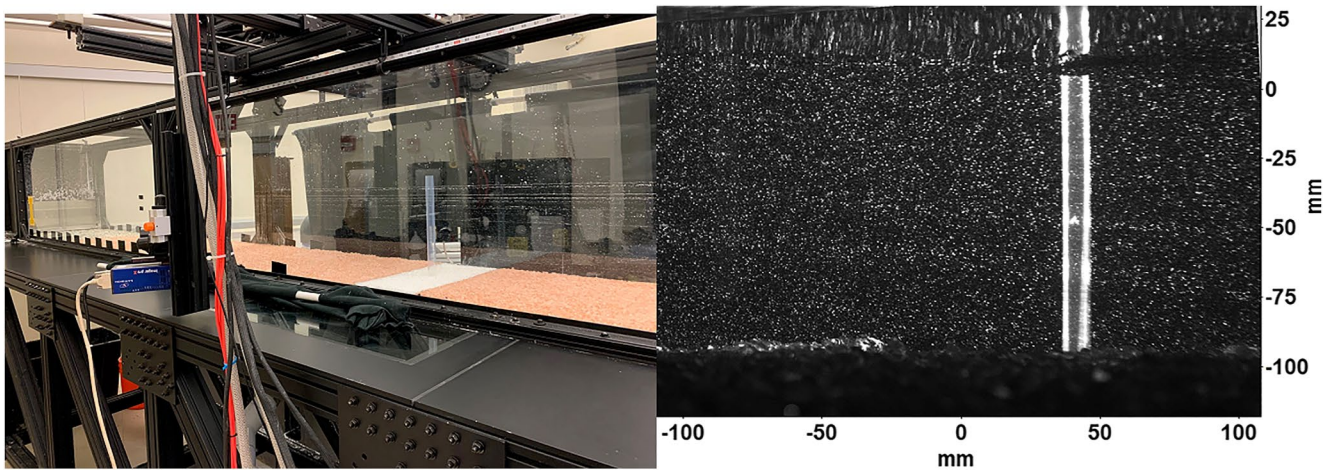

Figure 1. Experimental set up (left) with vertical cylinder and the distortion corrected stereo particle image velocimetry image (right).

and dynamic viscosity of 0.00297 kg·m^{-1} s^{-1} (Figure 1). The combination of RIM fluid and transparent cylinder enabled measurement of the full velocity field around the cylinder in one field of view using SPIV (Figure 1b).

The SPIV system consisted of LaVision Imager Pro X cameras fitted with Zhong Optics 35 mm f2 lenses, located on both sides of the flume in backscatter orientation. Laser illumination was provided by a Big Sky twin-pulsed, 250 mJ laser system with Quantel Ultra power supplies. Flow was seeded with a mixture of polymeric seeding particles, whose diameters ranged between 50 and 100 μm and densities between 1,000 to 1,200 kg m^{-3}, at approximately 10^8 particles m^{-3}. LaVision DaVis 8.4 software was used to control the system and analyze the PIV images. Image pairs were collected at approximately 11 Hz with a Δt of 2500 μs. Convergence analysis indicated that 2,000 image pairs were needed for each image plane to fully converge the measured and derived hydraulic quantities for each 0.15 m by 0.12 m field of view (Figure S3 in Supporting Information S1). Image planes were collected in two cross-stream transects (Figure S1 in Supporting Information S1). The upstream transect which, in the streamwise direction enclosed the stalk, consisted of 24 image fields. Near the stalk, image fields were spaced 2 mm apart. Spacing was increased to 4 mm further from the stalk. Image field locations ranged from 42 mm from the center of the stalk on the near side of the flume to 22 mm from center on the far side. The downstream transect, located 130 mm downstream of the main transect, consisted of three image fields at the stalk centerline and 4 mm cross-stream on both sided of center. Image fields were analyzed using DaVis 8.4 software with an interrogation window of 32 × 32 pixels (4 × 4 mm) with 75% overlap.

2.2. Data Analysis

The turbulent motion of an incompressible and Newtonian fluid is governed by the Reynolds averaged Navier Stokes, RANS, equations:

$$\frac{\partial \bar{u}_i}{\partial x_i} = 0 \qquad \text{Continuity equation} \tag{1a}$$

$$\rho \bar{u}_j \frac{\partial \bar{u}_i}{\partial x_j} = \rho \bar{f}_i + \frac{\partial}{\partial x_j}\left[-\bar{p}\delta_{ij} + \mu\left(\frac{\partial \bar{u}_i}{\partial x_j} + \frac{\partial \bar{u}_j}{\partial x_i}\right) - \rho\overline{u_i' u_j'}\right] \qquad \text{Momentum equations} \tag{1b}$$

where the subscripts i and j indicate the ith and jth directions, $i = 1, 2$ and 3 and $j = 1, 2$ and 3. The instantaneous velocity, u $(= \bar{u}_i + u_i')$, can be expressed with Reynolds decomposition as the sum between its turbulence-averaged expected value, $\bar{u}_i$ (mean), and fluctuations u_i' around the mean. The other quantities are the body force, f, in this case the acceleration of gravity, g, and ρ the fluid density. By using Equation 1a into 1b the gradient of the time-averaged pressure can be quantified as:

$$\frac{\partial \bar{p}}{\partial x_i} = \rho \bar{f}_i + \frac{\partial}{\partial x_j}\left[\mu\left(\frac{\partial \bar{u}_i}{\partial x_j} + \frac{\partial \bar{u}_j}{\partial x_i}\right) - \rho\overline{u_i' u_j'}\right] - \rho \bar{u}_j \frac{\partial \bar{u}_i}{\partial x_j} \tag{2}$$

Equation 2 can be expanded for instance in the 1–2 plane, for example, longitudinal, 1, and vertical, 2, directions, respectively, with 3 indicating the transversal direction, to identify the pressure gradient components easily:

$$\frac{\partial \bar{p}}{\partial x_1} = \rho \bar{f}_1 + \mu \left(\frac{\partial^2 \bar{u}_1}{\partial x_1^2} + \frac{\partial^2 \bar{u}_1}{\partial x_2^2} + \frac{\partial^2 \bar{u}_1}{\partial x_3^2} \right) - \rho \left(\frac{\partial \overline{u_1'^2}}{\partial x_1} + \frac{\partial \overline{u_1' u_2'}}{\partial x_2} + \frac{\partial \overline{u_1' u_3'}}{\partial x_3} \right) - \rho \left(\bar{u}_1 \frac{\partial \bar{u}_1}{\partial x_1} + \bar{u}_2 \frac{\partial \bar{u}_1}{\partial x_2} + \bar{u}_3 \frac{\partial \bar{u}_1}{\partial x_3} \right) \quad (3a)$$

$$\frac{\partial \bar{p}}{\partial x_2} = \rho \bar{f}_2 + \mu \left(\frac{\partial^2 \bar{u}_2}{\partial x_1^2} + \frac{\partial^2 \bar{u}_2}{\partial x_2^2} + \frac{\partial^2 \bar{u}_2}{\partial x_3^2} \right) - \rho \left(\frac{\partial \overline{u_1' u_2'}}{\partial x_1} + \frac{\partial \overline{u_2'^2}}{\partial x_2} + \frac{\partial \overline{u_2' u_3'}}{\partial x_3} \right) - \rho \left(\bar{u}_1 \frac{\partial \bar{u}_2}{\partial x_1} + \bar{u}_2 \frac{\partial \bar{u}_2}{\partial x_2} + \bar{u}_3 \frac{\partial \bar{u}_2}{\partial x_3} \right) \quad (3b)$$

which show the 4 terms quantifying the pressure gradients: the body force ($\bar{f}_i$, first term in the RHS of the equation), the viscous terms ($\mu \frac{\partial^2 \bar{u}_i}{\partial x_j x_j}$, the second term in the RHS of the equation), the turbulence, that is, the gradient of the Reynolds stress terms ($\frac{\partial}{\partial x_j}\left(-\rho \overline{u_i' u_j'}\right)$, the third term in the RHS of the equation) and the advective term ($-\rho \bar{u}_j \frac{\partial \bar{u}_i}{\partial x_j}$, the fourth term in the RHS of the equation), respectively.

SPIV technique provides instantaneous velocity in all three directions over a single plane such that all terms except those with derivatives in the out of plane direction (e.g., $\partial/\partial x_3$) can be quantified directly from the measurements by using the Reynolds decomposition. We quantified the out of plane gradients (e.g., $\partial/\partial x_3$) of the mean velocity and the Reynolds shear stress terms from the 24 closely spaced and aligned parallel planes (Figure S1 in Supporting Information S1). This allowed us to fully characterize all the right-hand terms in Equation 3. The accurate evaluation of each term requires their convergence, which requires sufficient number of images taken (Figure S3 in Supporting Information S1). Once the system is ergodic, the moments of the frequency distribution of the velocity remains constant and thus each term can be accurately quantified.

Currently, three major methods are available for pressure reconstruction based on SPIV measurements once the pressure gradient ($\nabla \bar{p}$) is known: (a) the virtual boundary Omni-Directional Integration in its virtual boundary (Joshi et al., 2014; Liu & Katz, 2006, 2008; 2013) and the parallel ray approaches (Liu et al., 2016; Liu & Moreto, 2020); (b) the Poisson equation method (De Kat & Van Oudheusden, 2012; Gurka et al., 1999); and (c) least square reconstruction (or Direct Matrix Inversion) method (Wang et al., 2016; Zhang et al., 2020). The recent work of Liu and Moreto (2020, 2021) indicates that the omni-direction integration approach has better performance than the others. Thus, we adapted the parallel-ray omni-directional algorithm to reconstruct the pressure field. The pressure field reconstructed from the RIM-matched SPIV data includes the near-bed pressure field, which is important for benthic and hyporheic process as it drives hyporheic flows. When the SPIV view window also captures the flow in close proximity to the water surface elevation, then the pressure distribution along the top boundary of the reconstructed pressure field contains sufficient information that allows the reconstruction of the free water surface, assuming the pressure on the top boundary of the reconstructed pressure domain is balanced by the response of the local hydrostatic pressure enabled by the local gravitational potential brought by the local free surface elevation (though the local free surface is not resolved directly by the PIV measurement). In this case, direct independent measurements of the water surface profile can be used to validate and/or quantify the performance of the pressure reconstruction method. Uncertainty of the reconstructed pressure field was quantified by investigating the error propagation from the converged SPIV measurement data to the reconstructed pressure field (SI) (Liu, 2001; Liu & Moreto, 2020).

We used the reconstructed near-bed pressure field as the upper boundary condition of a three-dimensional groundwater model with a homogenous (hydraulic conductivity, $K = 0.01$ cm s^{-1}) and isotropic porous media to predict the hyporheic flows induced by the interaction between the barely submerged single stalk and surface flow with realistic dimensions, flow characteristics and streambed roughness. Modeled alluvial bed had 0.2 m thickness and 0.5 m width and 0.5 m length with impervious bottom and lateral sides and a pressure drop between upstream and downstream ends similar to the flume slope (0.003 m m^{-1}).

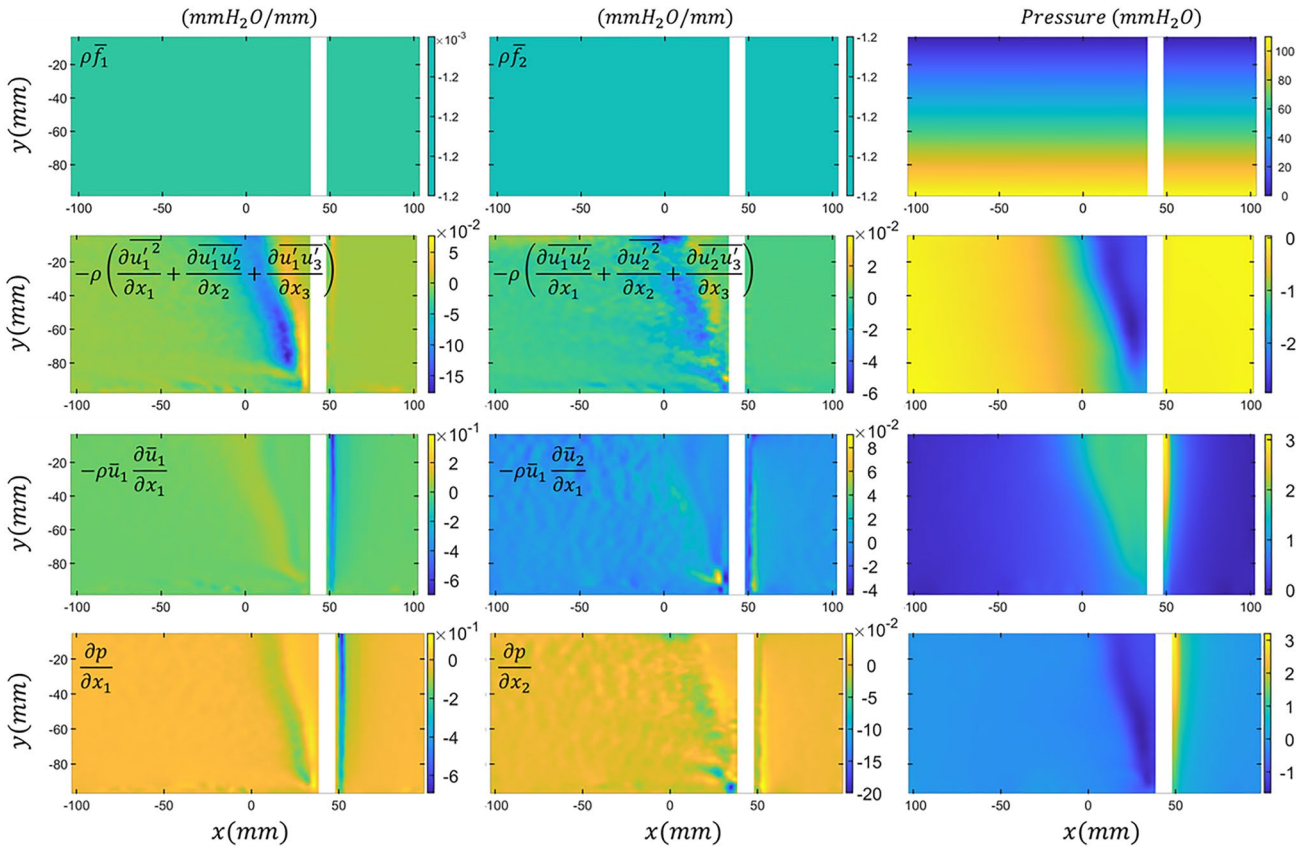

Figure 2. Distribution of the major RANS terms and the resulting pressure gradients (last row) quantified by stereo particle image velocimetry along the vertical plane passing through the stalk symmetry plane for Equation 3a, left column and Equation 3b, middle column, with the corresponding contributions to pressure shown in the right column. The white strip is the location of the stalk. All pressure gradient and its contributor terms are expressed as mmH_2O per mm. The bulk flow direction in from right to left.

3. Results and Discussion

The time averaged flow field measured by SPIV with the aforementioned measurement station setup allowed us to fully characterize the terms in Equation 3 (Figure S4 in Supporting Information S1) and identify the most important (Figure 2). By mapping their distribution, we identify locations of high and low turbulence stresses (gradients of the fluctuation velocity self- or cross-products), the distribution of viscous stresses (the term involving the dynamic viscosity) and the convection of momentum (the convective derivative of the time averaged velocity), which are important for near-bed transport of sediment. The ability to break down the pressure field by each component allows us to identify their relative importance, and how their relative importance changes spatially in the domain due to the presence of the stalk and bed roughness (Figure 2 and Figures S4–S6 in Supporting Information S1). Generally, the viscous stress term contribution (Figure S5 in Supporting Information S1 the second row from the top) is negligible to the final pressure distribution, p, (Figure S5 in Supporting Information S1 bottom right panel), because its effect is two orders of magnitude smaller than that of p. Interestingly, the dominant contributors to p are the streamwise advection term, $-\rho\bar{u}_1\frac{\partial\bar{u}_1}{\partial x_1}$, of the mean momentum (Figure 2, third row from the top; and Figure S4 in Supporting Information S1, eighth row from the top) and the out of plane derivative of the Reynolds stress term, $-\rho\frac{\partial\overline{u_1'u_3'}}{\partial x_3}$ (Figure 2, second row from the top; and Figure S4 in Supporting Information S1, seventh row from the top). The other terms, although important, have secondary effects as they are almost 1 order of magnitude smaller (Figure S6 in Supporting Information S1). Although the Reynolds stress $\overline{u_1'u_3'}$ is equal to 0 along the plane of geometric symmetry, its distribution in the wake is not symmetric through this plane, but instead anti-symmetric, for example, positive on one side and negative on the other through this plane, as shown by others (Braza et al., 2006; Thomas & Liu, 2004). Thus, its derivative is not 0 but it has a maximum value at the plane of symmetry. The terms $-\rho\bar{u}_1\frac{\partial\bar{u}_1}{\partial x_1}$ and $-\rho\frac{\partial\overline{u_1'u_3'}}{\partial x_3}$ are the major contributors

to the streamwise pressure gradient $\partial p/\partial x_1$, whereas the streamwise advection of the lateral momentum $-\rho\bar{u}_1\frac{\partial\bar{u}_2}{\partial x_1}$ and the Reynolds stress term $-\rho\frac{\partial\overline{u_2'u_3'}}{\partial x_3}$ are the major contributors to the vertical pressure gradient $\partial p/\partial x_2$ (Figure S4 in Supporting Information S1). The vertical convection $\bar{u}_2\frac{\partial}{\partial x_2}$ of the mean momentum (both $\rho\bar{u}_1$ and $\rho\bar{u}_2$ components) (Figure S4 in Supporting Information S1, ninth row from the top) contributes to p similarly. This result highlights the importance of a full 3-dimensional analysis of the problem in reconstructing the pressure field from the velocity fields and that of out-of-plane processes especially in the wakes of objects. Consequently, analyzing and understanding processes and mechanisms at the water-sediment interface where grains and macro-roughness features may form strong gradients in all directions may require full three-dimensional domain characterization. Error propagations estimated that the averaged error of the reconstructed pressure field is only 0.14% of the dynamic pressure for the current flow field investigated at a confidence level of 95% (Table S1 in Supporting Information S1). The corresponding absolute error for the reconstructed pressure is only 0.0334 Pa, that is, 0.0034 mmH_2O, which is 3 orders of magnitude smaller than the values of the reconstructed pressure field.

The pressure gradient distribution reveals the effect of the stalk on the pressure field, which exhibits high pressure on the upstream side and low pressure on the downstream and lateral sides of the stalk (Figures 3a–3c). The accelerated flow around the lateral sides of the stalk create pressure depressions at the sides of the base of the stalk that extend through the water column to the surface. This lowers the water surface elevation at either lateral side of the stalk (Figure 3e). The effect of the stalk on the near-bed pressure distribution persists nearly 8 D downstream, nearly 4 D on the sides and potentially 8 D upstream although our measurements stopped at 5 D upstream. To accent the small pressure changes caused by the stalk-flow interaction, we remove the effect of the body force, which would otherwise overwhelm and hide the pressure changes (cf., Figure S4 in Supporting Information S1 first row from the top). This pressure distribution is confirmed also by the ability of the omni-directional method to reconstruct the water surface elevation Δh with micro resolution (Figures 3a and 3e) when the SPIV image captures the free water surface. In this case, the pressure distribution reconstructed at the top of the flow field (top boundary Figure 3d) effectively delineates the water surface elevation (Figure 3e). As the flow approaches the barely submerged stalk, it decelerates and raises its water surface elevation (short-long dash blue line Figure 3a). Then the water accelerates over and around the stalk decreasing the water surface elevation downstream and along the stalk sides (Figure 3e). The rough streambed also causes a rough near-bed pressure distribution with smaller amplitude (~0.0032 mH_2O Figure 3a black solid line difference in pressure between upstream and downstream the stalk) compared to the water surface elevations difference between upstream and downstream the stalk (~0.0045 mH_2O, Figure 3a dark blue short-long dashed line). This underscores the difficulty to measure these quantities experimentally and here we provide a powerful and effective methodology, which can be used in large scale applications.

Although these near-bed pressure variations seem small (~0.003 mH_2O), their values are not too different from those caused by dune-like, for example, ripples and dunes, bedforms (Elliott & Brooks, 1997a) with similar surface hydraulics. They actually generate stronger gradient as the distance between high- and low-pressure points is shorter (~0.01 m across the stalk) (Figure 3a). Application of the near-bed pressure distribution as boundary condition of a groundwater model let us simulate the vegetation induced hyporheic flows, which formed multiple hyporheic exchange cells over a streambed area that extended 4·D on either side of the stalk and nearly 10·D upstream and downstream the stalk. The main hyporheic exchange cell moves water from upstream to downstream the stalk (Figure 3f), but lateral cells also move water toward the stalk. These hyporheic exchange cells have spatially averaged downwelling velocity of 1 cm hr^{-1} with homogeneous $K = 0.01$ cm s^{-1}. We compare this flux to that caused by a dune in dynamic equilibrium with the imposed flow depth. Such a dune would have a length and amplitude 6 and 0.167 time the mean flow depth (Yalin, 1964), respectively, thus 0.6 m long and 0.0167 m amplitude. By using Elliott and Brooks (1997a, 1997b) approach, this configuration generates a near-bed pressure variation of ~0.000017 mH_2O, which is 2 order of magnitudes smaller than that of the stalk (~0.003 mH_2O). Consequently, the ripple-induced mean downwelling velocity is 0.17 cm hr^{-1}, one order of magnitude smaller than that of the stalk.

In natural conditions, sediment transport would cause erosion and depositional processes around the stalk which would potentially lead to stronger hyporheic exchanges than those modeled here (Dudunake et al., 2020). Streambed heterogeneity, which we did not model here, may have limited impact in sand bedded streams (Tonina et al., 2016) but large in case of coarse-bed streams (Zhou et al., 2014). Besides, these limitations, our experimen-

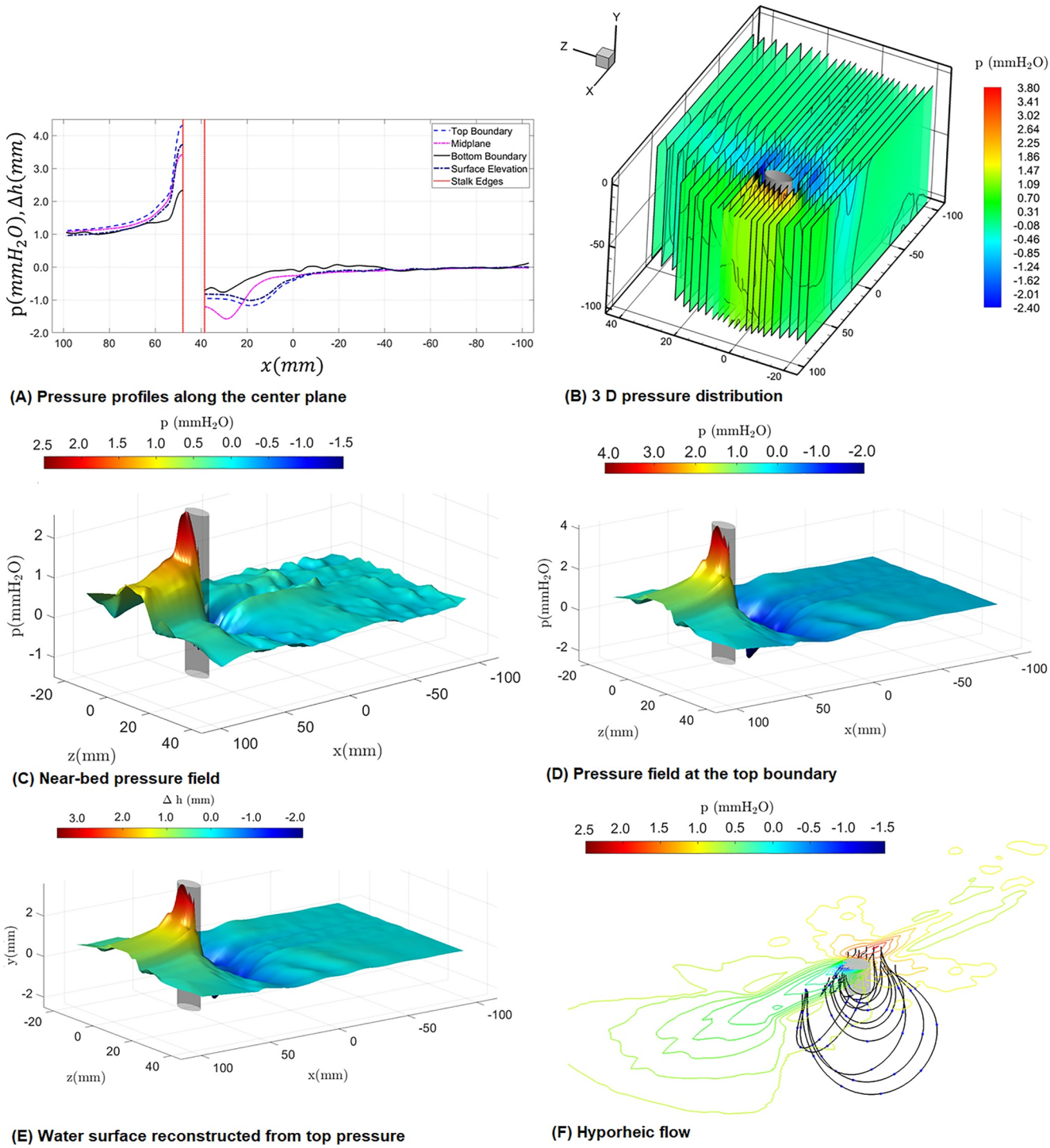

Figure 3. (a) Mean pressure distribution at different vertical location and water surface profile along the symmetry plane through the center of the cylinder. (b) Reconstructed 3D pressure distribution around the single stem, (c) Near-bed pressure distribution, (d) Pressure distribution at the top boundary of the flow field, (e) water free surface reconstructed from the top pressure distribution and (f) hyporheic flow lines around the stack which is identified by gray region. The bulk flow direction in from left to right.

tal results suggest that sparse rigid vegetation, like emergent pioneering plants on bars (Benjankar et al., 2014; Caponi et al., 2019), will enhance hyporheic exchange and its ecological benefits compared to unvegetated bars. They underscore and confirm the importance of vegetation in driving hyporheic flows as suggested by Yuan et al. (2021) based on numerical simulations of fully submerged canopy.

4. Conclusions

We reconstructed the full three-dimensional time-averaged pressure field around a barely submerged single vegetation stalk, simplified with a vertical rigid cylinder, over a rough bed made of irregular grains, which has never been done before. The pressure was reconstructed with the parallel-ray omni-directional integration algorithm from Reynolds-averaged flow field quantified with coupled refractive index matching (RIM) and stereo particle image velocimetry (SPIV). Our results show the feasibility of this approach, RIM-SPIV and parallel-ray omni-directional pressure reconstruction algorithm, to map the hydrodynamic and pressure fields and water surface elevation around solids experimentally with the use of low-cost and non-toxic fluids and solids in a real-scale flume experiment with rough beds and free water surface. Uncertainty analysis shows at a confidence level of 95% the averaged error of the reconstructed pressure field is only 0.14% of the dynamic pressure, which corresponds to an absolute error of 0.0034 mmH_2O and depends on the quality of the SPIV measurements. Thus, absolute error is 3 orders of magnitude smaller than the reconstructed pressure value. The analysis presented here can be extended to study flow and pressure fields around and within objects and structures for various hydraulic applications including studying forces on hydraulic structures, sediment grain mobility and transport and hyporheic exchange.

Extraction of the near bed pressure distribution from the full three-dimensional pressure field allowed quantifying the hyporheic fluxes generated by the stalk. The stalk-induced pressure field forms multiple hyporheic exchange cells within a streambed area extending nearly 10 times the stalk diameter, D, upstream and downstream the stalk and 4 D on either side. The barely submerged vegetation stalk induced 10 times stronger hyporheic fluxes than a dune-like bedform in dynamic equilibrium with the stream hydraulic conditions, experimentally demonstrating that emergent vegetations are key hyporheic driving mechanisms.

Conflict of Interest

The authors declare no conflicts of interest relevant to this study.

Data Availability Statement

Data, which are not published yet and properly cited, are available at Tonina, D., J. Moreto, W. J. Reeder, R. Budwig, X. Liu (2021). Data set: Experimentally mapping water surface elevation, velocity and pressure fields of an open channel flow around a stalk, HydroShare, http://www.hydroshare.org/resource/63ee32d2dff-f42129208acb8bd45c207.

Acknowledgments
We would like to thank the critical and constructive comments of the Editor Valeriy Ivanov and of an anonymous reviewer. This research was partially supported by Office of Naval Research ONR (N00014-19-1-2020, N00014-20-1-2276 and N00014-21-1-2392), the National Science Foundation NSF (Grants 1933176 and EAR1559348), the San Diego State University (UGP program 2015) for the pressure reconstruction method development and the USDA National Institute of Food and Agriculture, Hatch project 1012806. The views expressed in this article are those of the authors and do not necessarily represent the views or polices of funding agencies and institutions. Questions on the pressure reconstruction, the free-surface reconstruction and the uncertainty analysis could be addressed to Dr Xiaofeng Liu, xiaofeng.liu@sdsu.edu.

References

Benjankar, R., Burke, M., Yager, E., Tonina, D., Egger, G., Rood, S. B., & Merz, N. (2014). Development of a spatially-distributed hydroecological model to simulate cottonwood seedling recruitment along rivers. *Journal of Environmental Management*, *145*, 277–288. https://doi.org/10.1016/j.jenvman.2014.06.027

Blois, G., Best, J. L., Sambrook Smith, G. H., & Hardy, R. J. (2014). Effect of bed permeability and hyporheic flow on turbulent flow over bed forms. *Geophysical Research Letters*, *41*(18), 6435–6442. https://doi.org/10.1002/2014gl060906

Boano, F., Harvey, J. W., Marion, A., Packman, A. I., Revelli, R., Ridolfi, L., & Wörman, A. (2014). Hyporheic flow and transport processes: Mechanisms, models, and biogeochemical implications. *Reviews of Geophysics*, *52*(4), 603–679. https://doi.org/10.1002/2012RG000417

Bott, T. L., Kaplan, L. A., & Kuserk, F. T. (1984). Benthic bacterial biomass supported by stream water dissolved organic matter. *Microbial Ecology*, *10*, 335–344. https://doi.org/10.1007/bf02015558

Braza, M., Perrin, R., & Hoarau, Y. (2006). Turbulence properties in the cylinder wake at high Reynolds numbers. *Journal of Fluids and Structures*, *22*(6–7), 757–771. https://doi.org/10.1016/j.jfluidstructs.2006.04.021

Budwig, R. (1994). Refractive index matching methods for liquid flow investigations. *Experiments in Fluids*, *17*, 350–355. https://doi.org/10.1007/bf01874416

Caponi, F., Koch, A., Bertoldi, W., Vetsch, D. F., & Siviglia, A. (2019). When does vegetation establish on gravel bars? Observations and modeling in the Alpine Rhine River. *Frontiers of Environmental Science*, *7*, 124. https://doi.org/10.3389/fenvs.2019.00124

De Kat, R., & Van Oudheusden, B. W. (2012). Instantaneous planar pressure determination from PIV in turbulent flow. *Experiments in Fluids*, *52*, 1089–1106. https://doi.org/10.1007/s00348-011-1237-5

Dudunake, T., Tonina, D., Reeder, W. J., & Monsalve, A. (2020). Local and reach-scale hyporheic flow response from Boulder-induced geomorphic changes. *Water Resources Research*, *56*(10). https://doi.org/10.1029/2020WR027719

Edwards, R. T. (1998). The hyporheic zone. In R. J. Naiman, & R. E. Bilby (Eds.), *River ecology and management: Lessons from the Pacific coastal ecoregion* (pp. 399–429). Springer-Verlag. https://doi.org/10.1007/978-1-4612-1652-0_16

Elliott, A. H., & Brooks, N. H. (1997a). Transfer of nonsorbing solutes to a streambed with bed forms: Laboratory experiments. *Water Resources Research*, *33*(1), 137–151. https://doi.org/10.1029/96wr02783

Elliott, A. H., & Brooks, N. H. (1997b). Transfer of nonsorbing solutes to a streambed with bed forms: Theory. *Water Resources Research*, *33*(1), 123–136. https://doi.org/10.1029/96WR02784

Fehlman, H. M. (1985). *Resistance components and velocity distributions of open channel flows over bedforms*. Colorado State University.

Findlay, S., Strayer, W., Goumbala, C., & Gould, K. (1993). Metabolism of streamwater dissolved organic carbon in the shallow hyporheic zone. *Limnology & Oceanography*, *38*, 1493–1499. https://doi.org/10.4319/lo.1993.38.7.1493

Fischer, H. B., Kloep, F., Wilzcek, S., Push, M., & Pusch, M. T. (2005). A river's liver—Microbial processes within the hyporheic zone of a large lowland river. *Biogeochemestry*, *76*(2), 349–371. https://doi.org/10.1007/s10533-005-6896-y

Gibert, J., Stanford, J. A., Dole-Olivier, M.-J., & Ward, J. V. (1994). Basic attributes of groundwater ecosystems and prospects for research. In J. Gilbert, D. L. Danielpol, & J. A. Standford (Eds.), *Groundwater ecology* (pp. 8–40). Academic Press. https://doi.org/10.1016/b978-0-08-050762-0.50008-5

Gurka, R., Liberzon, A., Hefetz, D., Rubinstein, D., & Shavit, U. (1999). Computation of pressure distribution using PIV velocity data. In *3rd International workshop on particle image velocimetry*, 2, (pp. 1–6).

Hilliard, B., Reeder, W. J., Skifton, R. S., Budwig, R., Basham, W., & Tonina, D. (2021). A Biologically friendly, low-cost, and scalable method to map permeable media architecture and interstitial flow. *Geophysical Research Letters*, *48*(3), 1–9. https://doi.org/10.1029/2020gl090462

Joshi, P., Liu, X., & Katz, J. (2014). Effect of mean and fluctuating pressure gradients on boundary layer turbulence. *Journal of Fluid Mechanics*, *748*, 36–84. https://doi.org/10.1017/jfm.2014.147

Kim, B. K. A., Jackman, A. P., & Triska, F. J. (1992). Modeling biotic uptake by periphyton and transient hyporheic storage of nitrate in a natural stream. *Water Resources Research*, *28*(10), 2743–2752. https://doi.org/10.1029/92wr01229

Kim, T., Blois, G., Best, J. L., & Christensen, K. T. (2020). Experimental evidence of amplitude modulation in permeable-wall turbulence. *Journal of Fluid Mechanics*, *887*. https://doi.org/10.1017/jfm.2019.1027

Liu, X. (2001). *A study of wake development and structure in constant pressure gradients*. University of Notre Dame.

Liu, X., & Katz, J. (2006). Instantaneous pressure and material acceleration measurements using a four exposure PIV system. *Experiments in Fluids*, *41*(2), 227–240. https://doi.org/10.1007/s00348-006-0152-7

Liu, X., & Katz, J. (2008). Cavitation phenomena occurring due to interaction of shear layer vortices with the trailing corner of a two-dimensional open cavity. *Physics of Fluids*, *20*(4), 041702. https://doi.org/10.1063/1.2897320

Liu, X., & Katz, J. (2013). Vortex-corner interactions in a cavity shear layer elucidated by time-resolved measurements of the pressure field. *Journal of Fluid Mechanics*, *728*, 417–457. https://doi.org/10.1017/jfm.2013.275

Liu, X., & Moreto, J. R. (2020). Error propagation from the PIV-based pressure gradient to the integrated pressure by the omnidirectional integration method. *Measurement Science and Technology*, *31*(5), 055301. https://doi.org/10.1088/1361-6501/ab6c28

Liu, X., & Moreto, J. R. (2021). Pressure reconstruction of a planar turbulent flow field within a multiply connected domain with arbitrary boundary shapes. *Physics of Fluids*, *33*(10), 101703. https://doi.org/10.1063/5.0066332

Liu, X., Moreto, J. R., & Siddle-Mitchell, S. (2016). Instantaneous pressure reconstruction from measured pressure gradient using rotating parallel ray method, (pp. 1–8). In *54th AIAA Aerospace Sciences Meeting American Institute of Aeronautics and Astronautics*. https://doi.org/10.2514/6.2016-1049

Marion, A., Nikora, V. I., Puijalon, S., Bouma, T., Koll, K., Ballio, F., et al. (2015). Aquatic interfaces: A hydrodynamic and ecological perspective. *Journal of Hydraulic Research*, *52*(6), 744–758.

Marzadri, A., Dee, M. M., Tonina, D., Bellin, A., & Tank, J. L. (2017). Role of surface and subsurface processes in scaling N_2O emissions along riverine networks. *Proceedings of the National Academy of Sciences*, 114(17), 4330–4335. https://doi.org/10.1073/pnas.1617454114

Nepf, H. (2012). Flow and transport in regions with aquatic vegetation. *Annual Review of Fluid Mechanics*, *44*, 123–142. https://doi.org/10.1146/annurev-fluid-120710-101048

Ocampo, C. J., Oldham, C. E., & Sivapalan, M. (2006). Nitrate attenuation in agricultural catchments: Shifting balances between transport and reaction. *Water Resources Research*, *42*(W01408), 16. https://doi.org/10.1029/2004wr003773

Peralta-Maraver, I., Reiss, J., & Robertson, A. L. (2018). Interplay of hydrology, community ecology and pollutant attenuation in the hyporheic zone. *Science of the Total Environment*, *610*, 267–275. https://doi.org/10.1016/j.scitotenv.2017.08.036

Quick, A. M., Reeder, W. J., Farrell, T. B., Tonina, D., Feris, K. P., & Benner, S. G. (2016). Controls on nitrous oxide emissions from the hyporheic zones of streams. *Environmental Science and Technology*, *50*(21), 11491–11500. https://doi.org/10.1021/acs.est.6b02680

Rousseau, G., & Ancey, C. (2020). Scanning PIV of turbulent flows over and through rough porous beds using refractive index matching. *Experiments in Fluids*, *61*(8), 1–24. https://doi.org/10.1007/s00348-020-02990-y

Shen, G., Yuan, J., & Phanikumar, M. S. (2020). Direct numerical simulations of turbulence and hyporheic mixing near sediment-water interfaces. *Journal of Fluid Mechanics*, *892*. https://doi.org/10.1017/jfm.2020.173

Thomas, F. O., & Liu, X. (2004). An experimental investigation of symmetric and asymmetric turbulent wake development in pressure gradient. *Physics of Fluids*, *16*(5), 1725–1745. https://doi.org/10.1063/1.1687410

Tonina, D., & Buffington, J. M. (2009). A three-dimensional model for analyzing the effects of Salmon redds on hyporheic exchange and egg pocket habitat. *Canadian Journal of Fisheries and Aquatic Sciences*, *66*(12), 2157–2173. https://doi.org/10.1139/F09-146

Tonina, D., de Barros, F. P. J., Marzadri, A., & Bellin, A. (2016). Does streambed heterogeneity matter for hyporheic residence time distribution in sand-bedded streams? *Advances in Water Resources*, *96*, 120–126. https://doi.org/10.1016/j.advwatres.2016.07.009

Triska, F. J., Duff, J. H., & Avanzino, R. J. (1993). Patterns of hydrological exchange and nutrient transformation in the hyporheic zone of a gravel bottom stream: Examining terrestrial-aquatic linkages. *Freshwater Biology*, *29*, 259–274. https://doi.org/10.1111/j.1365-2427.1993.tb00762.x

van Oudheusden, B. W. (2013). PIV-based pressure measurement. *Measurement Science and Technology*, *24*(3), 032001. https://doi.org/10.1088/0957-0233/24/3/032001

Voermans, J. J., Ghisalberti, M., & Ivey, G. N. (2017). The variation of flow and turbulence across the sediment-water interface. *Journal of Fluid Mechanics*, *824*, 413–437. https://doi.org/10.1017/jfm.2017.345

Wang, Z., Gao, Q., Wang, C., Wei, R., & Wang, J. (2016). An irrotation correction on pressure gradient and orthogonal-path integration for PIV-based pressure reconstruction. *Experiments in Fluids*, *57*(6), 1–16. https://doi.org/10.1007/s00348-016-2189-6

Weitzman, J. S., Samuel, L. C., Craig, A. E., Zeller, R. B., Monismith, S. G., & Koseff, J. R. (2014). On the use of refractive-index-matched hydrogel for fluid velocity measurement within and around geometrically complex solid obstructions. *Experiments in Fluids*, *55*(12), 1–12. https://doi.org/10.1007/s00348-014-1862-x

Westerweel, J., Elsinga, G. E., & Adrian, R. J. (2013). Particle image velocimetry for complex and turbulent flows. *Annual Review of Fluid Mechanics*, *45*, 409–436. https://doi.org/10.1146/annurev-fluid-120710-101204

Yalin, M. S. (1964). Geometrical properties of sand waves. *Proceedings of the American society of civil engineers journal of the hydraulics division*, 90, 105–119. https://doi.org/10.1061/jyceaj.0001097

Yuan, Y., Chen, X., Cardenas, M. B., Liu, X., & Chen, L. (2021). Hyporheic exchange driven by submerged rigid vegetation: A modeling study. *Water Resources Research*, *57*(6). https://doi.org/10.1029/2019WR026675

Zarnetske, J. P., Haggerty, R., Wondzell, S. M., & Baker, M. A. (2011). Dynamics of nitrate production and removal as a function of residence time in the hyporheic zone. *Journal of Geophysical Research*, *116*(G1), G01025. https://doi.org/10.1029/2010JG001356

Zhang, J., Brindise, M. C., Rothenberger, S., Schnell, S., Markl, M., Saloner, D., et al. (2020). 4D flow MRI pressure estimation using velocity measurement-error-based weighted least-squares. *IEEE Transactions on Medical Imaging*, *39*(5), 1668–1680. https://doi.org/10.1109/TMI.2019.2954697

Zhou, Y., Ritzi, R. W., Soltanian, M. R., & Dominic, D. F. (2014). The influence of streambed heterogeneity on hyporheic flow in gravelly rivers. *Ground Water*, *52*(2), 206–216. https://doi.org/10.1111/gwat.12048

Ziebis, W., Forster, S., Huettel, M., Jørgensen, B. B., & Jorgensen, B. B. (1996). Complex burrows of mud shrimp Callianassa Truncata and their geochemical impact in the sea bed. *Nature*, *382*(6592), 619–622. https://doi.org/10.1038/382619a0

References From the Supporting Information

Figliola, R. S., & Beasley, D. E. (2015). *Theory and design for mechanical measurements* (6th edn). John Wiley and Sons.

Liu, X. (2001). *A study of wake development and structure in constant pressure gradients*. University of Notre Dame.

Liu, X., & Moreto, J. R. (2020). Error propagation from the PIV-based pressure gradient to the integrated pressure by the omnidirectional integration method. *Measurement Science and Technology*, *31*(5), 055301. https://doi.org/10.1088/1361-6501/ab6c28